Automatic Setup and Calibration of a Robotic PIV System using Fiducial Markers

F. Michaux[1,*], A. Brunn[1], C. Willert[2], S. Kallweit[1,3,*]

1: 1) iLA_5150 GmbH, Germany
2: DLR Institute of Propulsion Technology, German Aerospace Center, Germany
3: University of Applied Sciences in Aachen, Germany
*Corresponding author: michaux@ila5150.de

Keywords: PIV calibration, automation, robotics, fiducial marker system, recognition algorithms.

ABSTRACT

The use of industrial robots allows the precise manipulation of all components necessary for setting up a large-scale particle image velocimetry (PIV) system. The known internal calibration matrix of the cameras in combination with the actual pose of the industrial robots and the calculated transform from the fiducial markers to camera coordinates allow the precise positioning of the individual PIV components according to the measurement demands. In addition, the complete calibration procedure for generating the external camera matrix and the mapping functions for e.g. dewarping the stereo images can be automatically determined without further user interaction and thus the degree of automation can be extended to nearly 100%. This increased degree of automation expands the applications range of PIV systems, in particular for measurement tasks with severe time constraints.

1. Introduction

The use of fiducial markers is standard in a wide variety of robotic or automated applications, mostly for perception and localization procedures. There are different families of markers (Garrido-Jurado et al., 2014; Zakiev et al., 2020) where the properties can be tailored to the application, e.g. visibility, size, additional information content, detection speed and detection stability (Krogius et al., 2019). Common to all optical markers is the use of a monocular camera image, providing the complete 6D pose of the depicted marker. As a result, the transformation between the camera and marker coordinates is available. With the known internal camera matrix, which can be easily calculated from the data sheet of the used camera and a high-quality lens, the 6D pose of a given marker, such as an *AprilTag* (Olson, 2011), can be determined and used for latter calibration or positioning routines. The higher detection uncertainty of the pose of one marker and possible occlusions lead to the application of a bundle of markers. So a checkerboard with *AprilTag* or *ArUcoTag* markers is used to allow the 6D pose estimation of the complete calibration grid in camera coordinates as shown in Fig. 1. The known 6D pose of the robots in world coordinates are then

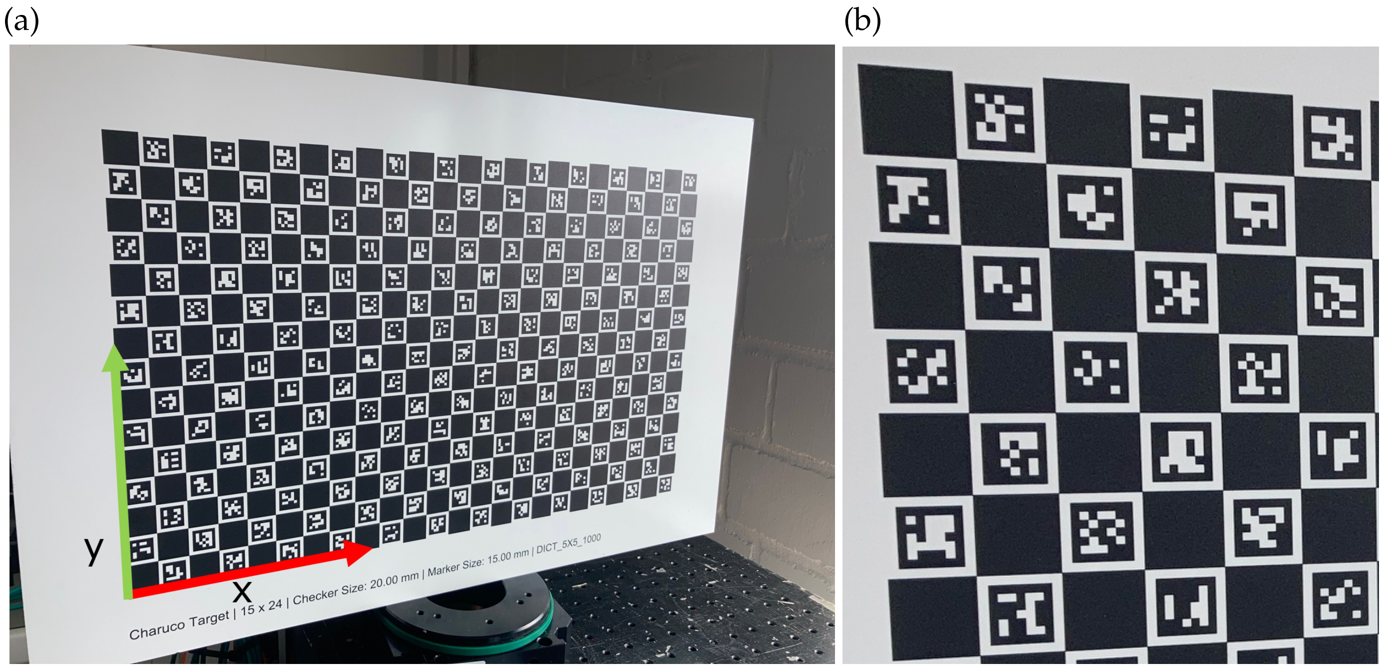

Figure 1. Calibration checkerboard (a) (*ChArUco*) with *ArUcoTag* bundle. (b) detail showing individual *ArUco* tags of type DICT_5x5_1000 each with 5×5 bit encoding.

used to calculate the transforms from robot coordinates to target coordinates in order to control individual camera-robot positions and the robot for the light sheet optics allowing an optimal setup for the measurement task.

2. Procedure

The automated calibration procedure starts by placing the calibration grid with the *ArUcoTag* bundle at the measurement position. The calibration grid consists of a combination of ArUco (Garrido-Jurado et al., 2014) and standard checker board markers - so called *ChArUco* grids (Fig. 1). A first estimate of the camera pose from the calibration grid image is determined and used to move the camera-robot accordingly. The marker detection algorithm provides a transform of the marker bundle coordinate frame shown in (Fig. 1) to the camera coordinate system. By using the known static transform from robot tool center point (TCP) to camera frame, the camera can now be translated and rotated to the desired position in robot coordinates. So, the optimal camera and light sheet angles can be automatically adjusted. When the set of cameras – in our case two for a standard stereoscopic approach – are aligned to the target, the known number and size of the calibration square points, which are encoded in the chosen tag family, are back-projected to the calibration grid in order to calculate the mapping function. Here, the artificial markers of the calibration procedure are placed close enough to the checkerboard corners, so that the exact location of these corners can be determined afterwards via a gradient-based sub-pixel algorithm (Fig 3).

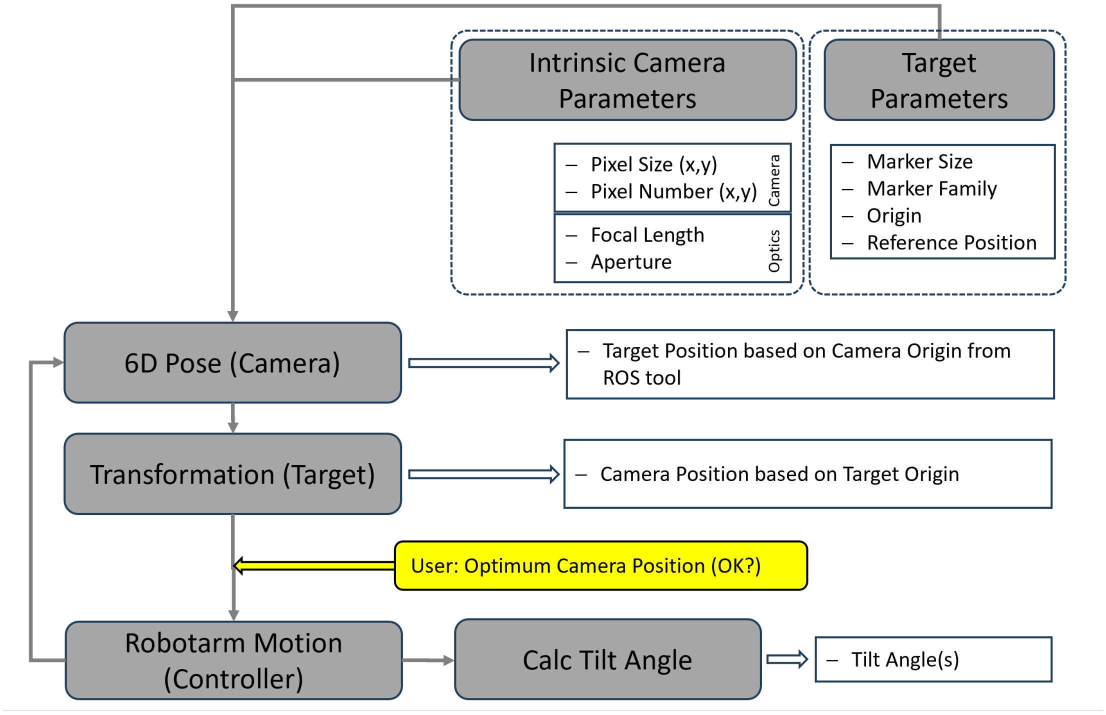

Figure 2. Scheme of a typical calibration process

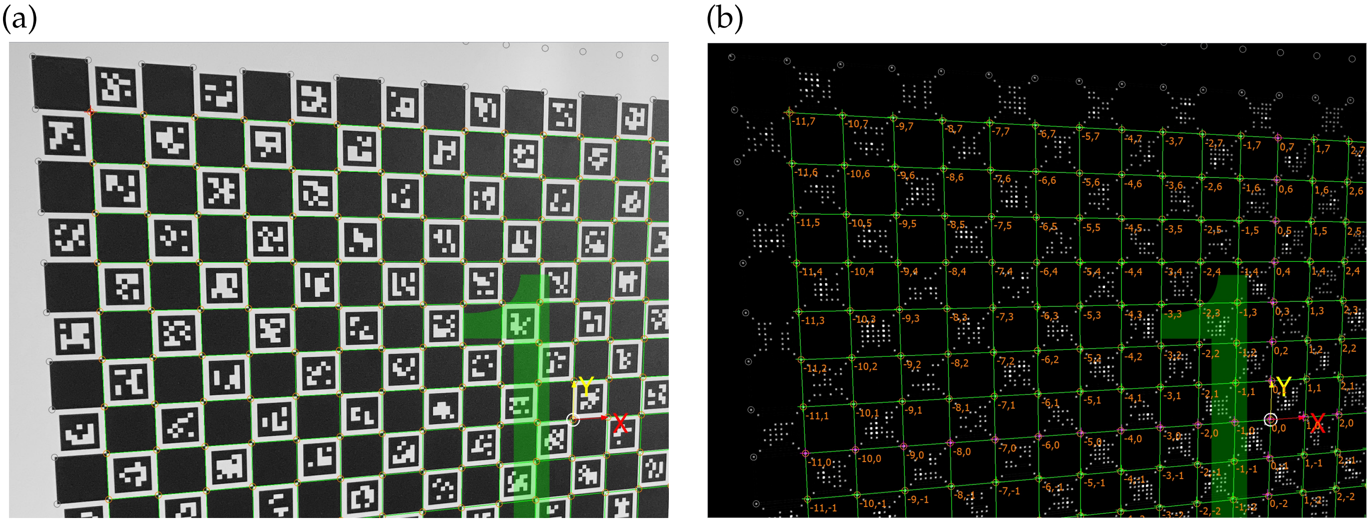

Figure 3. Automated grid registration using sub-pixel accurate corner detection. (a) original image with overlaid grid, (b) image after applying corner detection and grid reconstruction.

The control of the light sheet robot is done according to the described procedure. To align the light sheet even closer to the calibration target, the disparity map is used to calculate the translation and orientation of the light sheet in respect to the calibration grid. This information can be used in a closed loop control system.

The proposed method only needs a modified calibration rig, providing the necessary optical markers in order to allow the transform from one coordinate frame into another. The markers can either be printed on existing calibration grids or new modified calibration grids can be used. No active lighting is required; ambient lighting conditions are sufficient to capture images of the target as input to the described calibration procedure. In addition, the markers can be used to encode information into the calibration grid to trigger certain pre-programmed behaviors, allowing a complete automatic setup and calibration procedure using industrial robots. Even in configurations where robots for camera and laser positioning are not available, the method can be used to precisely align the PIV setup manually or with a motorized traversing unit based on the real time camera pose estimation of the marker detection algorithm.

Only parts of the complete ChAruCo target need to be visible in the camera frame in order to detect the target pose - an important advantage of the proposed method. The individual ArUco markers on the calibration grid are used to generate a list of real world and pixel point correspondences for the latter PIV mapping function. Here the real world coordinates of the checker board corners are back-projected to pixel coordinates with the known transform of the 6D pose in camera coordinates.

3. Experimental Setup

For determining the measurement deviation according to DIN 1319 (DIN, 1995), every measurement value has a systematic known and an unknown (random) deviation. The random deviation can be estimated by statistical means, often called 'repeatability' in data sheets. The measurement uncertainty is based on statistical evaluation of the measurement results by using the standard deviation s and providing a level of confidence. The level of confidence is simply the amount of measurement values (percentage) in the Gaussian distribution of the measurement results of the used sensor, so e.g. 68% for ± one standard deviation s (U68), or 95% for $\pm 2s$ (U95) (JCGM, 2008). U95 is used for most of the engineering applications because a value of 5% outliers can be accepted in most industrial applications. The complete measurement value always consists of the measured value from the device and an uncertainty with an assigned level of confidence - in our case U95. In order to estimate the systematic deviation and the uncertainty of pose measurements using a ChArUco calibration target, a calibration standard - a Faro measuring arm is used (Platinum 2.4m, Fig. 4). The Faro arm has an U95 of 25 µm for point measurements and 36 µm for volumetric measurements (Faro, 2010) determined by using a procedure for estimating the measurement uncer-

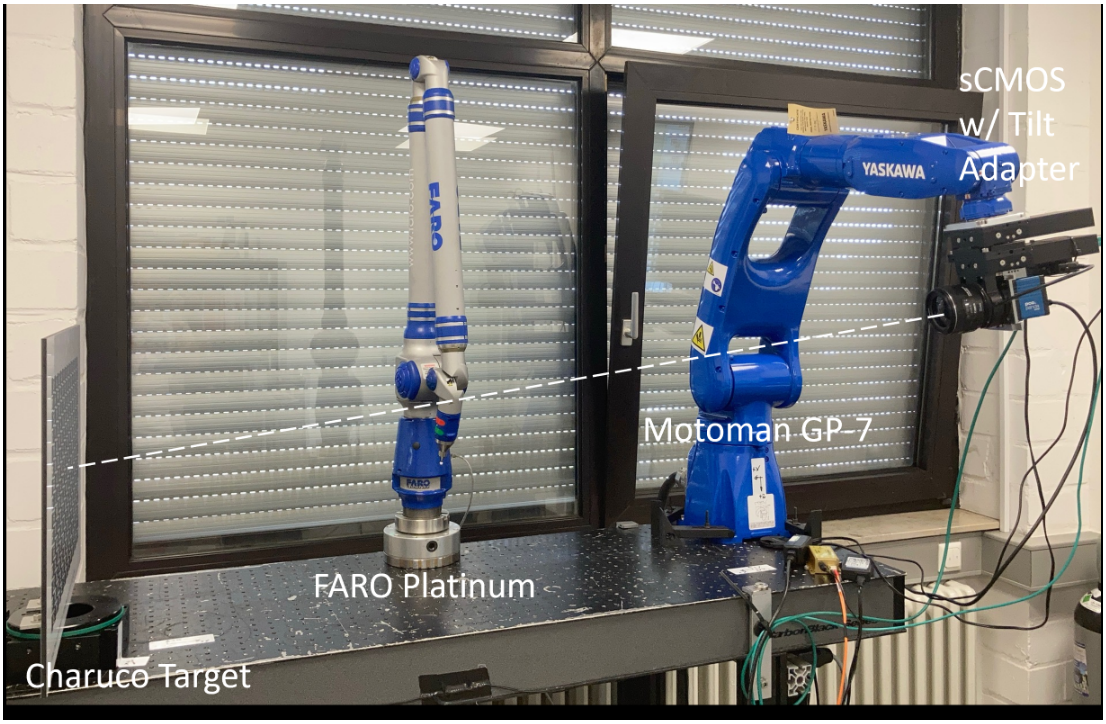

Figure 4. sCMOS camera mounted on GP-7 robot arm rotated around x and y axis, pointing towards the center of the ChArUco target plate. FARO measuring arm was used as position reference.

tainty for articulated arm coordinate measuring machines described in (Dain Johnson, 2019). The measurement arm is calibrated before using as described in the user manual and placed between the ChArUco target and the camera system. The camera is a pco panda DS26 with 2×2 binning enabled, resulting in a 2560×2560 resolution. A Canon USM 35 mm lens with $f\#$ 1:2 is placed on a motorized tilt mount in front of the panda at 44 mm back focal length - the standard for Canon SLR lenses. Focusing is done via a remote focus ring controlling the focus and the aperture of the USM lens. The target is focused with complete open aperture and then later closed to an $f\#$ of 5.6, which is a reasonable value for enough focal depth for analyzing the inclined target plane even under tilt angles (around the target y axis) of up to 70°. A standard ChArUco target with 15×24 markers with a checker marker size of 20 mm and an ArUco marker size of 15 mm (DICT_5x5_1000, Fig. 1) is used. The target is fixed to a motorized turn table with a resolution of 0.01°and a repeatability of 0.001°.

In order to enable rotation around the x axis and the y axis of the target, the camera was mounted on a robot arm (YASKAWA Motoman GP-7) and aligned to the center of the target. In addition this setup is used for validating the translational deviation along the x and y axis of the target. The positioning repeatability of the GP-7 is ±10 µm according to ISO 9283 standards. The robot controller is enabling rotation around the center of the ChArUco target by using so called 'user frames'.

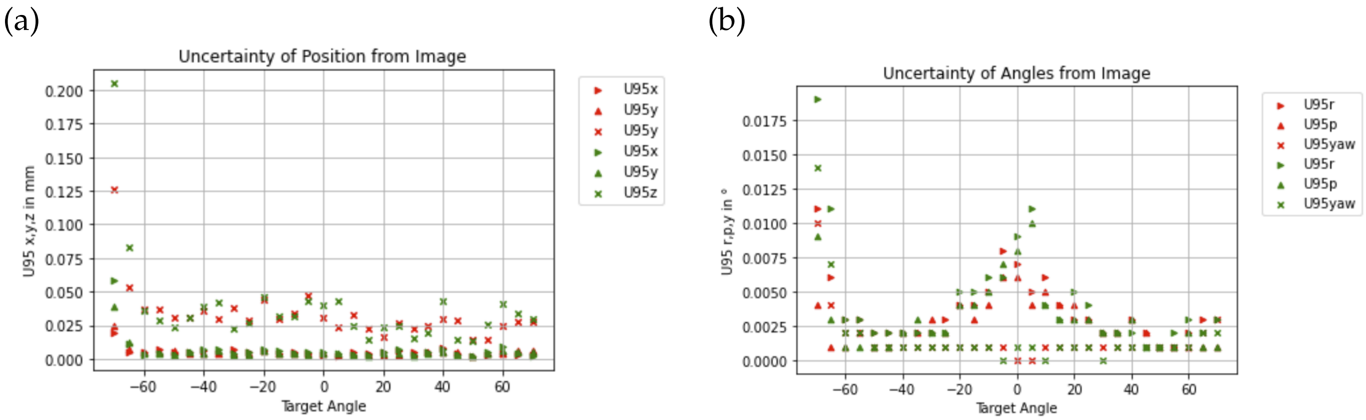

Figure 5. Uncertainty (repeatability) from single images (a) position, (b) angle.

The complete tool chain of identifying the pose of the target is implemented in the Robot Operation System (ROS) (Stanford Artificial Intelligence Laboratory et al., 2020) by using the charuco_detector package (Carlos da Costa, 2022) which generates a 6D pose of the target in camera coordinates. The measurements are generated using two calibration files: one with the theoretical values of the camera intrinsic matrix (NoCalib) and one with the intrinsic matrix from a calibration with a standard 5×7 checker board with 25 mm squares (Calib). The theoretical values for the NoCalib intrinsic matrix, so fx, fy, cx, cy are calculated from the focal length of the used Canon lens and the center ray fixed to the geometric center of the sensor at (1280, 1280). The 6D pose is calculated from 100 images. The U95 of the pose estimate for a single image are calculated for x, y and z positions and the angles roll r, pitch p and yaw, shown in Fig 1.

For testing the stability of the pose estimate with only a couple of markers in the field of view (FOV), the camera was moved parallel along the target. The minimum number of markers for a valid detection is four, so at least a 3×3 subgroup of the target. In addition the camera was inclined by a roll angle (around the target x axis) of 15°and then tilted to angles up to ±70°.

All poses (inclination angles and positions) are referenced by the Faro arm, where ten points are acquired on the target itself for determining the plane and the left lower corner - the origin of the ChArUco target shown in Fig 5. The coordinates from each point are again the average of ten single measurements. The flatness of the acquired planes is checked and was less than 100 µm for the complete experiment. The pose of the camera is as well referenced by the Faro using a special tool mounted at the imager plane of the camera.

4. Results

The measurement uncertainty U95 being two times the standard deviation is only valid for a Gaussian distribution of the measurement data. In order to test for normality, a Shapiro-Wilk test is used

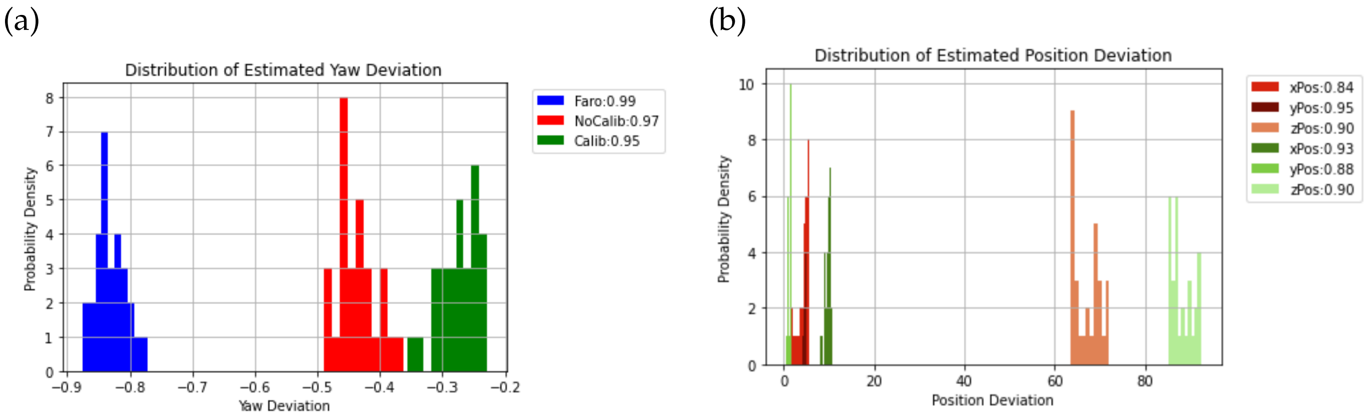

Figure 6. Probability density of (a) yaw angle deviation, (b) position deviation.

from the SciPy.stats statistics package (The SciPy community, 2024). The probability density function of the estimated yaw angle and position distribution is shown in (Fig 6), where the values in the legend are the Shapiro test results. Values close to 1.0 and higher than 0.8 indicate a Gaussian distribution. So the following measurement uncertainties can be calculated assuming a normal distribution of the data sets.

When comparing the results of the estimation of the yaw angle of the inclined ChArUco target, a higher deviation of the calibrated camera can be seen (Fig. 7). All three data sets provide slightly lower values for the yaw angle. Here the turn table was used as a reference.

When calculating the average values over all measured angles and the uncertainties, which are now including the systematic deviations, the following table is generated:

System	Mean to Turn Table	U95 to Turn Table	Mean to Faro	U95 to Faro
Calib	-0.27°	0.06°	0.56°	0.06°
NoCalib	-0.44°	0.06°	0.39°	0.07°
Faro	-0.83°	0.05°	NA	NA

The Faro results have a nearly constant systematic deviation of around -0.8° to the turn table because there was no initial referencing made to match turn table and Faro angle. The calibrated camera produces a slightly lower deviation to the turn table reference than the non-calibrated camera but is further away from the Faro (Fig. 7). The positional derivations can only be referenced to the Faro system, so that all following measurement data is referenced to the Faro measurement arm.

Comparing the deviation of the target position from the marker detection with the Faro data reference generates the following table, where all values are in [mm]:

System	D_x	$U95_{Dx}$	D_y	$U95_{Dy}$	D_z	$U95_{Dz}$
Calib	9.71	1.40	1.32	0.63	88.27	4.79
NoCalib	4.41	2.22	4.71	0.44	67.14	5.77

The conclusion is quite obvious: the calibrated camera produces a higher systematic deviation for the x position and as well for the z position estimate, whereas the y deviation is a little lower. The uncertainty of both systems are in the same range but the deviation of the non-calibrated camera has a lower range (Fig. 8). The deviation in z position for both systems can be explained by the camera pinhole model used for calculating the 3D to 2D point transform for imaging applications.

The origin of the camera coordinate frame is in the center of the lens package – not in the center of the detector array – so the sensor distance z_{sd}, where the camera coordinate frame origin for referencing with the measuring arm is located, can be calculated by adding the back focal length b_{fl} to the focal length f of the used lens:

$$z_{\text{sd}} = f + b_{\text{fl}} \tag{1}$$

With the common value $b_{\text{fl}} = 44\,\text{mm}$ and $f = 35\,\text{mm}$, $z_{\text{sd}} = 79\,\text{mm}$ which is near to the experimental value of around 67 mm. The Canon data sheet provides a length of 62.5 mm for the lens, so the center of the lens package can be estimated to be at around 31 mm from the end of the mounting flange, resulting in a sensor distance of $z_{\text{sd}} \approx 78\,\text{mm}$.

When comparing the position deviation as a function of the inclined yaw angle, it is obvious that the calibrated camera has a larger deviation from the reference than the non-calibrated data. Another visible effect is the dependency of the x position deviation from the inclination angle, whereas the y position is not strongly influenced by the yaw angle. After validating the procedure with the explained method, some additional measurements are made using the setup depicted in

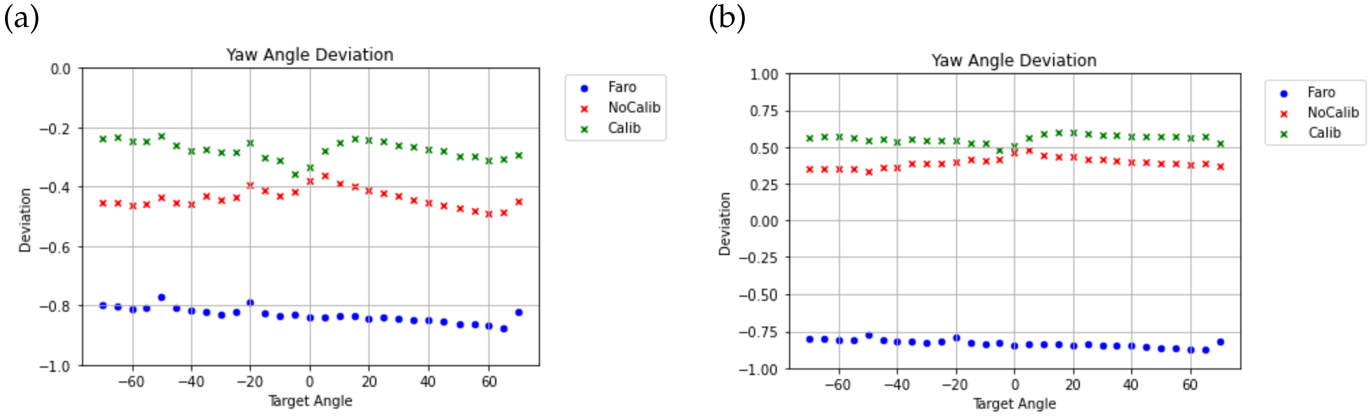

Figure 7. Yaw angle deviation (a) referenced to turn table, (b) referenced to Faro arm.

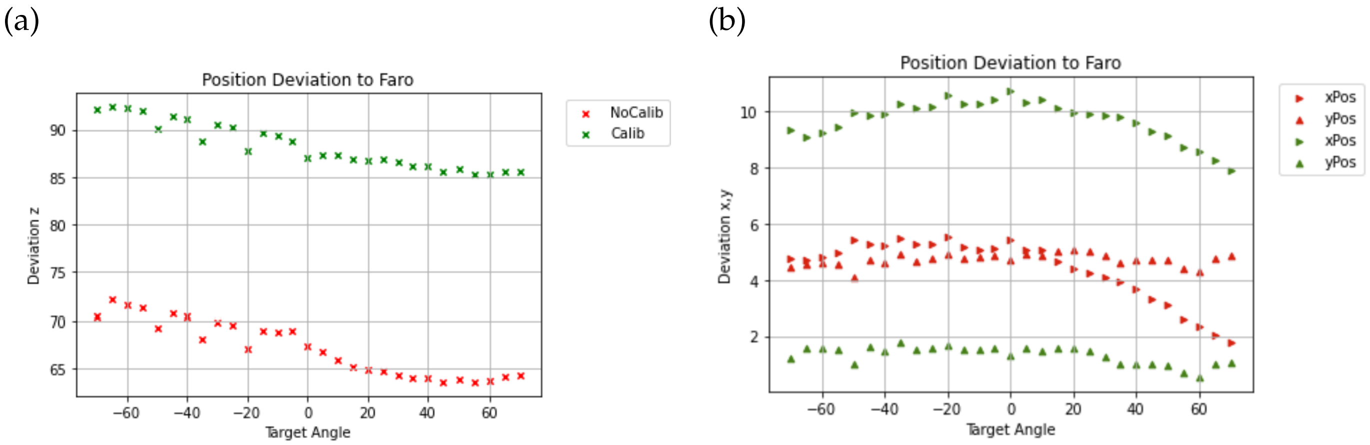

Figure 8. Position deviation: green is Calib, red NoCalib (a) z position, (b) x, y position

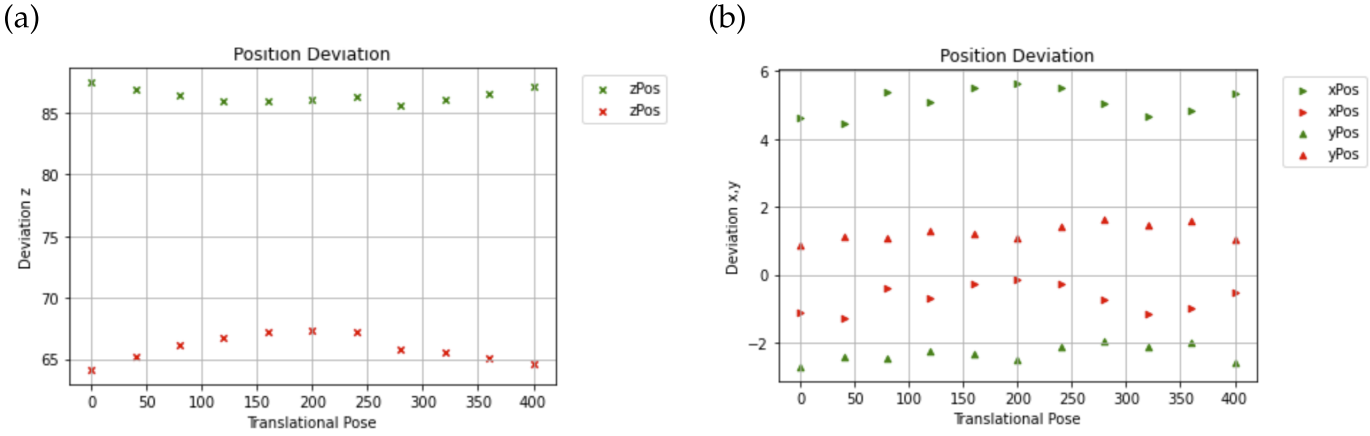

Figure 9. Translational pose deviation: green is Calib, red NoCalib (a) z position, (b) x, y position

Fig. 4 by moving the camera to different poses with an inclined ChArUco target. The origin of the coordinate frame for the robot was placed in the center of the ChArUco target. The pose of the camera is always referenced to the Faro measurement arm as described before and the origin of the ChArUco target is still at the depicted location from Fig 1.

First the camera is only moved parallel to the target with no tilt angle in x direction until no more valid detection is possible, so less than four markers are visible. The deviation in the z position is very similar to the previous experiment, whereas the x and y position deviation is lower than for the inclined tests (Fig. 9).

For the inclined pose estimation test with two angles (roll, r, kept constant and pitch, p, variable), the non-calibrated camera data was used due to the smaller deviation compared to the calibrated system. The camera was pointing at the target with a roll angle (around the x axis) of $r = 15°$. At an inclination angle (pitch around $y$axis) of 0°, the camera is first aligned to acquire the complete target with 100% visibility of the markers. Afterwards the target is rotated by 15, 25, 40, 50 and

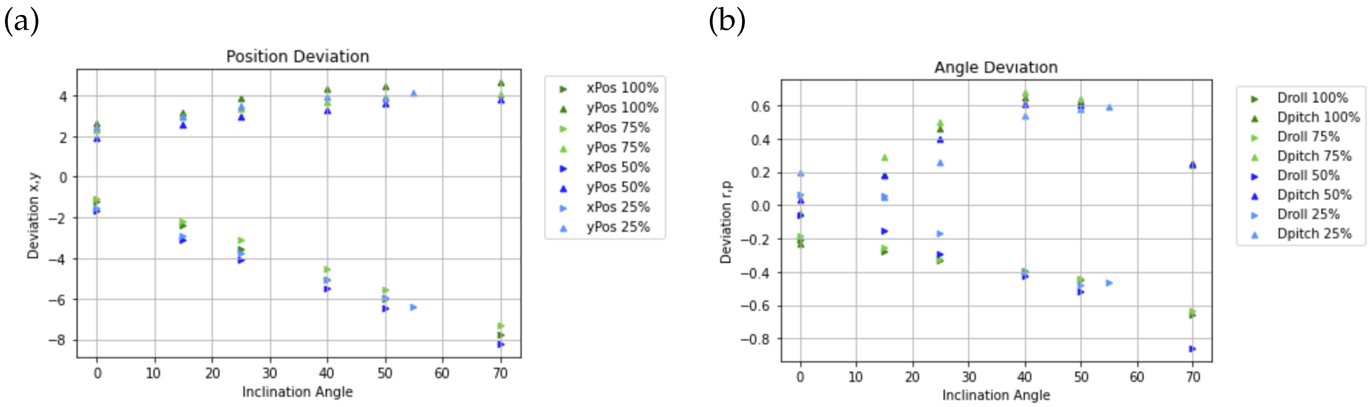

Figure 10. Rotational Pose deviation (a) x, y position, (b) roll r, pitch p angles

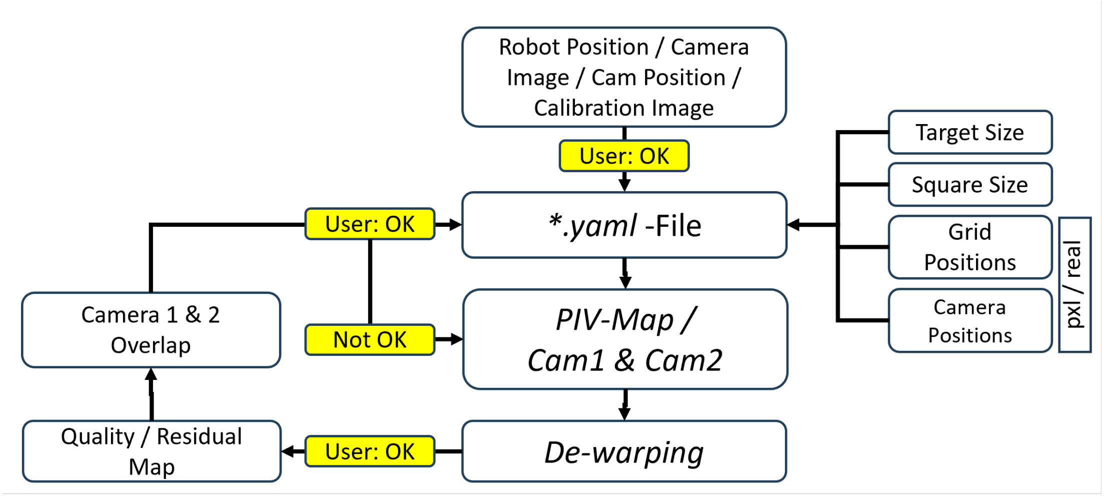

Figure 11. Workflow of calibration within the software environment of *PIVView 4.0*

70°. Then the camera is translated, so that only 75% of the markers are visible at 0° tilt (pitch) angle. This is repeated for 50% and 25% visibility of the markers, where at 25% the pitch angle was reduced to a maximum of $p = 55°$. At higher angles not enough markers are visible.

As seen in Fig. 10 the deviation in x position is even for high tilt angles of 50° in the range of $5 - 6\,\text{mm}$ where the y position deviation is a little lower. Looking at the estimated angles, the deviation for roll is around -0.5° for tilt angles in the 50° range and nearly the same for pitch with around +0.6°.

5. Conclusions

The use of fiducial markers can simplify the setup of a PIV system tremendously. Even the process of camera calibration with standard checker boards in order to get the intrinsic camera matrix can be skipped. For a camera with a nearly distortion free SLR lens and known pixel size and image sensor dimensions, the intrinsic parameters can be retrieved from the corresponding data sheet. With a measurement uncertainty of around 2.5 mm in x, 0.5 mm in y and 6 mm in z, the camera coordinates can be estimated quite well for most of the PIV setups with a working distance in a range of around 2 m. The estimation of the roll and tilt angle is in a remarkable low area of around 0.5°for mostly used tilt angles lower than 50°and even suitable at high tilt angles around 70°for back-scatter PIV setups. If the estimation deviates in a larger than mm range, the camera can be moved in steps to the target position by considering the first estimation of the camera pose and correcting the pose accordingly, even if the markers are not completely visible. It turns out that less than 50% of the board markers are sufficient for a reliable detection of the calibration grid with tilt angles of up to 70°. An estimation of the uncertainty at larger working distances can be made by using a laser tracker as reference. Nevertheless, the camera needs to be calibrated for e.g. the de-warping procedure for stereo PIV after positioning by generating a mapping function with the necessary point correspondences. But even here, the use of a calibration target with fiducial markers allows the complete automatic calibration (Fig. 11) by detecting the marker IDs and the corresponding corners for determining the real world/pixel coordinates correspondences by back-projection of the known corner positions. As a final step in the calibration, a disparity correction based on recorded particle images accounts for the residual misalignment between laser light sheet and calibration target.

References

Carlos da Costa. (2022). charuco_detector.. Retrieved from `https://github.com/carlosmccosta/charuco_detector`

Dain Johnson. (2019). Calibration of articulating arm coordinate measuringmachines per asme b89.4.22-2004. In *19th international congress of metrology, 09005 (2019).* doi: https://doi.org/10.1051/metrology/201909005

DIN. (1995). Grundlagen der Messtechnik - Teil 1: Grundbegriffe..

Faro. (2010). Faroarm platinum, 2.4m.. Retrieved from `https://www.faro.com/measuring-arms`

Garrido-Jurado, S., Muñoz-Salinas, R., Madrid-Cuevas, F., & Marín-Jiménez, M. (2014). Automatic generation and detection of highly reliable fiducial markers under occlusion. *Pattern Recognition*, *47*(6), 2280-2292. Retrieved from `https://www.sciencedirect.com/science/article/pii/S0031320314000235` doi: 10.1016/j.patcog.2014.01.005

JCGM. (2008). Evaluation of measurement data — Guide to the expression of uncertainty in measurement.. doi: https://doi.org/10.59161/JCGM100-2008E

Krogius, M., Haggenmiller, A., & Olson, E. (2019). Flexible layouts for fiducial tags. In *2019 IEEE/RSJ International Conference on Intelligent Robots and Systems (IROS)* (p. 1898–1903). IEEE Press. Retrieved from `https://doi.org/10.1109/IROS40897.2019.8967787` doi: 10.1109/IROS40897.2019.8967787

Olson, E. (2011). AprilTag: A robust and flexible visual fiducial system. In *2011 IEEE International Conference on Robotics and Automation* (p. 3400-3407). doi: 10.1109/ICRA.2011.5979561

Stanford Artificial Intelligence Laboratory et al. (2020). Robotic operating system.. Retrieved from `https://www.ros.org`

The SciPy community. (2024). scipy.stats.shapiro.. Retrieved from `https://docs.scipy.org/doc/scipy/reference/generated/scipy.stats.shapiro.html`

Zakiev, A., Tsoy, T., Shabalina, K., Magid, E., & Saha, S. K. (2020). Virtual experiments on ArUco and AprilTag systems comparison for fiducial marker rotation resistance under noisy sensory data. In *2020 International Joint Conference on Neural Networks (IJCNN)* (p. 1-6). doi: 10.1109/IJCNN48605.2020.9207701